Novel $Ir_{1-x}Co_xO_2$ thin films: Growth and characterization

M.A. Laguna–Marco [a,b,*], J. Herrero-Albillos [a,c], M.H. Aguirre [a,b,d], M. Rueda-Jiménez [c],
I. Mikulska [e]

[a] *Instituto de Nanociencia y Materiales de Aragón (INMA), CSIC – Universidad de Zaragoza, 50009 Zaragoza, Spain*
[b] *Departamento de Física de la Materia Condensada, Universidad de Zaragoza, 50009 Zaragoza, Spain*
[c] *Departamento de Ciencia y Tecnología de Materiales y Fluidos, Universidad de Zaragoza, Zaragoza 50018, Spain*
[d] *Laboratorio de Microscopías Avanzadas, Universidad de Zaragoza, 50018 Zaragoza, Spain*
[e] *Diamond Light Source Ltd Harwell Science and Innovation Campus Didcot, Oxfordshire OX11 0DE, UK*

ABSTRACT

$Ir_{1-x}Co_xO_2$ thin films have been prepared by reactive co–sputtering deposition at room temperature. Composition, structure, electronic properties and electric and magnetic behavior have been analyzed by different techniques including XRR, XRD, TEM microscopy, SQUID magnetometry, electrical resistivity and XAS spectroscopy. After annealing, an $Ir_{1-x}Co_xO_2$ substitutional solid solution phase with rutile crystal structure was achieved for a wide Co-doping range $0 \leq x \leq 0.6$. Starkly departing from the highly insulating behavior of CoO and Co_3O_4, the electrical resistivity at room temperature of our films is only slightly higher than that of IrO_2. Likewise, our work shows that the magnetic response of the doped films is very similar to that of the paramagnetic parent IrO_2. Neither ferromagnetism nor enhanced paramagnetism is observed. XAS spectra indicate a Co^{3+} oxidation state and, correspondingly, an oxidation state of ~5+ for Ir ions in the polycrystalline $Ir_{0.6}Co_{0.4}O_2$ film. By application of sum rules, a 13 % increase in the spin–orbit coupling is found despite the lattice shrinkage causes a detrimental bandwidth broadening.

1. Introduction

IrO_2 is currently one of the most promising materials for spin–current detection applications due to the high spin–orbit coupling (SOC) of the Ir ions, which makes possible an efficient conversion of pure spin-currents on charge-currents via the so-called inverse spin Hall effect (ISHE) [1,1,2,2]. The performance of IrO_2 as spin detector is found to be even better in the amorphous state [1,1] and this improvement has been proposed to be rooted to the increased Ir-O bond lengths [3,3]. To further optimize the performance of IrO_2 doping with different elements appears as a natural route. Indeed, in the current quest for optimized spintronic materials, doping is one of the most feasible and commonly used methods to modify the electronic structure of the host compounds [4–10,4–10]. The different ionic size of the dopant may give rise to contraction/elongation of the lattice and/or distortions that can significantly change the electronic structure. Similarly, the dopant ions can induce relevant changes in the oxidation state of the host. In addition, when a magnetic ion is inserted in the lattice it can give rise to the appearance of magnetic ordering [4,4,11]. To date the doping with 4 +

ions has been reported to give rise to strong changes in the electronic and magnetic behavior of IrO_2. Thus, Sn^{4+} has proven to result in a significant enhancement of the resistivity associated to the enlargement of the lattice and the closed-shell electronic configuration of Sn^{4+} [3,3]. Cr^{4+} doping has been reported to induce the appearance of magnetic ordering in the paramagnetic host and a magnetic moment of Ir^{4+} with an unusual spin-character [11,11]. On the other hand, to the best of our knowledge, no works aimed at increasing the oxidation state of Ir in IrO_2 films have been carried out to date even when in other iridium oxide series, Ir^{5+} shows a higher SOC than Ir^{4+} [12,12].

Despite the strong value of the SOC in IrO_2 it has to be noted that the electronic structure of IrO2 is markedly different to that found in other iridates, such as such as the Ruddlesden-Popper series, where the SOC plays a key role. In IrO_2 there is a high connectivity based on a 3D corner-sharing and edge-sharing octahedral network. This results in a relatively large value of the bandwidth W and a concomitant small effective correlation, U/W, so that the strong SOC is not responsible for any of the major features of the band structure in IrO_2. In other words, IrO_2 presents a metallic and paramagnetic ground state where the $J_{eff} =$

1/2 state is not relevant [13,13,14,14].

Interestingly enough, IrO_2 is also considered a state-of-the-art oxygen reduction reaction (OER) catalyst because it combines a good OER performance and high stability [15] [15]. In this research area doping has been also proved to be a viable approach to improve its intrinsic properties as Cu, Ce, Ga, Ni, Cr, Mn, Fe, Co or Ni have been tested [15–20,15–20]. However, despite the large number of works carried out in the last decade trying to better understand the relationships between crystallographic structure, electronic structure and OER performance, the mechanisms responsible for the improvement of the catalytic activity of IrO_2 are still a matter of debate and intense study. In many of these works the dopant element is not proved to enter in the host lattice or the synthesis method lead to relative small dopant amounts inserted in the lattice. This shortage is reported to limit the OER performance [16,16]. Regarding the role of the Ir valence, the enhanced performance of pseudo-amorphous IrO_2 points to the coexistence of Ir^{4+} and Ir^{3+} ions as a key factor according to Elmaalouf et al. and González et al. [21,21, 22,22]. Contrariwise, other works suggest that the presence of shorten of Ir–O metal ligand bonds and the increment of iridium oxidation state could lead to superior OER ability [23,23,24,24].

Here, Co-doped IrO_2 thin films have been grown aiming at obtaining a well-defined solid solution phase with high atomic substitution of the Ir content. Therefore, special attention was paid to ensure that (i) the dopant does not form secondary phases but enters in the lattice substituting Ir ions and (ii) the amount of Co in the lattice is maximized. Taking into account the most common oxidation states of Co, i.e. 2 + and 3 +, such a doping is expected to trigger an increase in the oxidation state of Ir so a ~ 5 + is obtained for a particular doping amount: nominally, 50 % doping in the case of Co^{3+} and 33 % doping for Co^{2+}.

2. Method

$Ir_{1-x}Co_xO_2$ thin films were prepared by reactive magnetron co–sputtering deposition on Si substrates at room temperature (RT) from metallic Ir and Co targets connected to a DC and a pulsed DC source, respectively. For the growth of the $Ir_{0.95}Co_{0.05}O_2$ film two DC sources were used. The power supplied to the Ir target was set to ~8 W. The sputtering power supplied to the Co target was varied from 7 W to 60 W to obtain dilutions with different Ir/Co ratio, ranging from 5 to 60 at % Co. The gas flows were set to 13 ml Ar/min and 2 ml O_2/min. The amorphous as–grown films were subsequently annealed in air at 600 ºC during 6 h to obtain polycrystalline samples. Given the technological interest of amorphous IrO_2, in some samples no thermal treatment was carried out. It should be noted that, for a given Co content, as-grown and annealed samples were grown simultaneously in order to ensure same Co doping. Pure IrO_2, grown by the same sputtering process, was used as reference.

Relative quantification of concentration of cobalt and iridium (in atomic %) has been calculated from XPS (X-Ray Photoelectron Spectroscopy) spectra of regions Co 2p 3/2 and Ir 4 f. The XPS analyses were carried out with a Kratos Axis SUPRA spectrometer using a monochromatic Al Kα source (5 mA, 15 kV). X–ray reflectivity (XRR) and X–ray diffraction (XRD) measurements were performed at room temperature on a Bruker D8 X–ray diffractometer and a *Rigaku* D/Max Ru300 diffractometer, respectively, by using the Kα radiation line of copper. The resistivity measurements were carried out in a PPMS 9 T and the magnetic measurements in a SQUID magnetometer MPMS–XL (both from Quantum Design). Transmission electron microscopy images, HRTEM (High resolution transmission electron microscopy) and STEM-HAADF (scanning TEM with high angular annular dark field detector), were performed by Tecnai F30 and Titan G2 80–300 keV (with aberration corrected probe), respectively, operated at 300 keV (Thermo Fisher Scientific, MA, USA). The compositional analysis profile was performed by energy dispersive spectroscopy (EDS) in an Oxford Aztec equipment in situ STEM-HAADF analysis. The lamellae for TEM analysis were prepared by focused ion beam in a Helios 650 N dual beam

equipment (Thermo Fisher Scientific).

X–ray absorption spectroscopy (XAS) measurements were carried out at the B18 beamline of the Diamond Light Source. Co K-edge and Ir $L_{2,3}$-edge XAS spectra of the films were measured in fluorescence mode using Quick-EXAFS technique. A Si (111) double crystal monochromator was used to select the incident X-ray energy. Co K-edge (Ir L_3-edge) measurements have been performed using collimating mirror with Pt (Cr) coating. The fluorescence measurements have been performed using Canberra 36-pixel Monolithic Segmented Hyper Pure Germanium Detector with the STFC Xspress4 Digital Pulse Processor [25,25]. The energy calibration for Co K-edge and Ir L_3-edge XAS measurements was established with simultaneous absorption measurements on 5 μm-thick Co and Pt metal foils.

3. Results and discussions

As summarized in Table 1, we have grown thin films with ~70 nm thickness and a roughly evenly–spaced Co dopant content in the ~ 5 – 60 at % range, relative to the total Ir + Co content. The as-grown films are amorphous, but after annealing the $Ir_{1-x}Co_xO_2$ films exhibit a polycrystalline non–textured microstructure, as shown in Fig. 1(a). All the samples crystallize in the rutile–type structure ($P4_2/mnm$ space group) even when no binary Co oxide crystallizes in this structure. No Bragg peaks were observed on a film with 70 % Co substitution (not shown). Diffraction peaks corresponding to the most common binary Co oxides, namely CoO and Co_3O_4, are not discerned in any sample.

As the Co content increases position of the Bragg peaks progressively shifts to higher angles, indicating a progressive contraction of the lattice (see Fig. 1). A nearly linear decrease of the cell volume with the Co doping is obtained. Therefore, our XRD measurements indicate that, when sputtered in an O_2–rich atmosphere, Ir and Co form a $Ir_{1-x}Co_xO_2$ substitutional solid solution phase with no critical concentration limiting the substitution of dopant into the lattice in the 0 < x < 0.6 range. This is the first report on the successful synthesis of polycrystalline $Ir_{1-x}Co_xO_2$ thin films. Moreover, when compared to the few works reported on powdered samples [16–18,26,16–18,26], a higher Co content and/or a better-defined location of Co dopant ions is found. This indicates that sputtering is more effective in introducing Co ions into the IrO_2 lattice than chemical reduction, Pechini and hydrothermal methods.

The unit cell contraction rate observed is ~ 1.3 % for every 10 % Co substitution. This contraction is similar to that found for Cr doping [11, 11] and, as in the Cr case, should be rooted in the smaller size of the Co ionic radius relative to Ir^{4+} (0.625 Å) [27,27]. In this sense, it is worth noticing that the rutile structure, with edge–sharing octahedra, is quite rigid compared, for instance, to perovskites and not as susceptible to distortion via inter–octahedral M–O–M tilting (M = Ir, Co). A revision of the size of the different Co ionic radius allow us to straightforwardly discard the presence of Co^{2+} (0.65 Å in low spin state (LS) and 0.75 Å in high spin state (HS)). The presence of Co^{3+} ions in HS state is also unlikely as its ionic size (0.61 Å) is similar to that of Ir^{4+} and so a smaller

Table 1

Structural and compositional properties of the polycrystalline $Ir_{1-x}Co_xO_2$ thin films: nominal stoichiometry, layer thickness (*t*) measured by XRR, Co concentration determined by XPS (relative to the total Ir + Co content) and lattice parameters obtained from XRD.

Sample	*t* (nm) (± 1 nm)	Co (%) (± 5 %)	*a* = *b* (Å)	*c* (Å)
$Ir_{0.95}Co_{0.05}O_2$	72	4	4.466(5)	3.11 (1)
$Ir_{0.9}Co_{0.1}O_2$	77	12	4.460(5)	3.10 (1)
$Ir_{0.8}Co_{0.2}O_2$	72	20	4.453(5)	3.09 (1)
$Ir_{0.7}Co_{0.3}O_2$	73	34	4.430(5)	3.07(1)
$Ir_{0.6}Co_{0.4}O_2$	65	41	4.40(1)	3.08 (1)
$Ir_{0.5}Co_{0.5}O_2$	99	48	4.42(2)	3.03(2)
$Ir_{0.4}Co_{0.6}O_2$	77	65	4.40(1)	3.00(2)

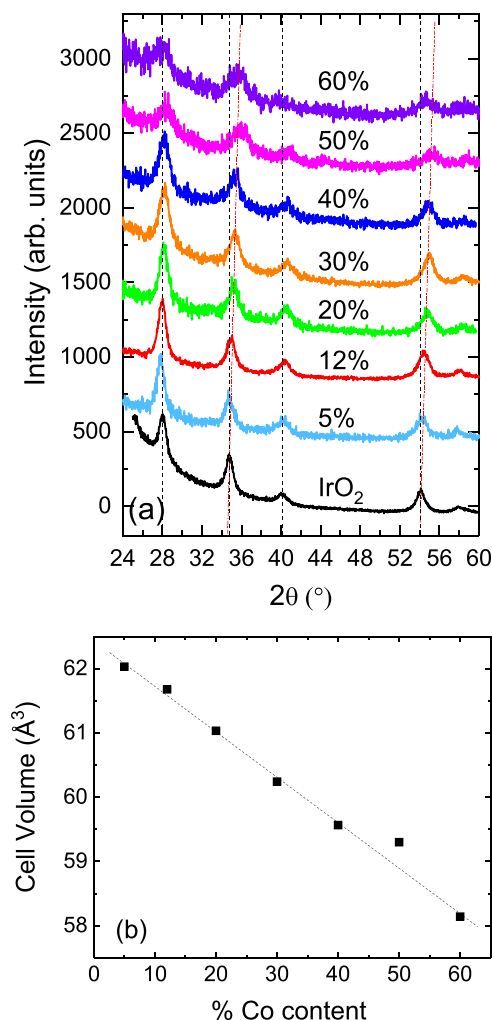**Fig. 1.** (a) XRD patterns for annealed $Ir_{1-x}Co_xO_2$ thin films. The diffractograms are vertically shifted for the sake of clarity. The dashed black lines mark the position of the diffraction peaks measured on IrO_2 while the red dotted lines are a guide to the eye. (b) Dependence of the cell volume with the Co–concentration. The dotted line is a guide to the eye.

contraction, would be expected. On the other hand, the ionic radius of both Co^{3+} (LS) (0.545 Å) and Co^{4+} (0.53 Å) is in agreement with the cell contraction observed. Previous works have revealed that doping with larger Sn^{4+} (smaller Cr^{4+}) ions causes an expansion (contraction) of the IrO_6 octahedra [3,3,11]. Consequently, a Co^{3+} doping seems more likely than a Co^{4+} one since a smaller ionic radius (0.57 Å for Ir^{5+}) better fit the shorter Ir-O bond distances in the doped samples. It is worth mentioning at this point that the synthesis of bulk samples via Pechini method is reported to result in a different oxidation state for cobalt, Co^{2+} [26,26].

The evolution of the peak width indicates a roughly constant decrease of the grain size from $\sim$ 8 nm to $\sim$ 4 nm, as derived from Scherrer equation, i.e., a progressive reduction of the crystallinity as Co content increases. The additional presence of increasing inhomogeneity in the composition of the grains and/or the coexistence of differentiated crystalline and amorphous regions cannot be ruled out. However, the gradual decrease of the grain size along with the nearly linear decrease of the cell volume with the Co doping supports that the main effect of doping on the microstructure is a gradual amorphization.

Therefore, XRD data confirm that polycrystalline $Ir_{1-x}Co_xO_2$ films have been successfully grown for the first time. In addition, a large substitution of Ir by Co, $0 \leq x \leq 0.6$, has been proved. Indeed, when compared to the few works reported on powdered samples [16–18,26,

16–18,26] a higher Co content and/or a better-defined location of Co dopant ions is found. This indicates that sputtering is more effective in introducing Co ions into the IrO_2 lattice than chemical reduction, Pechini and hydrothermal methods. The synthesis of bulk samples via Pechini method also results in a different oxidation state for cobalt, Co^{2+} [26,26].

TEM data confirm the thickness and homogeneity of the films, the average size of the crystalline nanograins obtained by XRD and the percentage of Co and its uniform distribution through the film. As can be seen in Fig. 2, grains of $\sim$4 nm can be identified for high doping (nominal 40 % Co); The EDS linescan in-situ STEM-HAADF confirms the percentage and homogeneity of doping.

The electrical resistivity $\rho(T)$ curves, displayed in Fig. 3(a), show a change in electrical behavior from the well-known metallic behavior of IrO_2, i.e. $d\rho/dT > 0$, to a typical semiconducting thermal dependence, i.e. $d\rho/dT < 0$. However, it should be noticed that the increase of the resistivity at room temperature relative to IrO_2 is small, only a factor 8 higher for the 50 % doped sample. Moreover, the increase of resistivity as the temperature decreases is very small, R(5 K)/R(300 K) < 1.2. From this slight dependence it can be concluded that typical resistivity models such as the thermal activation or the 3D Mott's variable range hopping (Mott–VRH) are not suitable to explain these data. Whereas the presence of localization mechanism(s) hindering the movement of the electrons in the doped samples can be clearly concluded from the data in Fig. 3(a), neither correlations (Mott insulator) nor magnetism (see Fig. 4) seem to be the underlying mechanism.

Based on the reduction of crystallinity and the increasing inhomogeneity observed by XRD, we propose the change in electrical resistivity to be associated to disorder introduced by the presence of Co atoms. In addition, structural distortions driven by the compression of the lattice may also be playing a role in this behavior. Moreover, the $\rho(T)$ curves corresponding to 5 % and 20 % doping (see Fig. 4(b)) show the appearance of clear upturns (marked with arrows in the figure) that are observed at increasing temperatures as the Co content is increased. Similar response has been reported for Cr-doped films [11,11] and for compressed $SrIrO_3$ thin films [28,28] and associated to disorder as localization mechanism hindering the movement of the electrons. In those works, the behavior in the low temperature region of resistivity curves showing an upturn has been accounted for in terms of weak (Anderson) localization, a disorder–driven effect due to quantum interference of the conducting charge carriers at defect sites [29,29].

For the sake of completeness, it is interesting to highlight the stark difference with the insulating CoO and Co_3O_4 compounds, with band gap > 0.6 eV and $\rho > 1$ Ωcm [30–33,30–33]. In addition, given the technological interest of amorphous IrO_2, the resistivity of the amorphous 40 % Co-doped IrO_2 film was also recorded. Also in this case the electrical transport behavior is slightly semiconducting.

Regarding the magnetic response, no hint of ferromagnetic (FM) response is observed in the $Ir_{1-x}Co_xO_2$ samples (Fig. 4). This magnetic behavior largely differs from the ferromagnetism observed in similar systems such as Cr-doped IrO_2 [11,11] and Co-doped SnO_2 [34,34] thin films. Moreover, no enhancement of the magnetic susceptibility is observed. As can be seen in Fig. 4, the paramagnetic susceptibility of the Co-doped compounds is very similar to that of the pure IrO_2, whereas a noticeable enhancement of the magnetic susceptibility would be expected if the Co ions bore any sizable magnetic moment as that expected for Co^{2+}, Co^{4+} or Co^{3+} HS. Indeed, an order of magnitude increase in the magnetic susceptibility is reported for bulk Co^{2+}-doped IrO_2 [26,26]. Therefore, the magnetic response observed in Fig. 4 is a strong evidence of a Co^{3+} ($3d^6$) LS electronic configuration.

In an attempt to confirm the formation of Co^{3+}, the Co K-edge XAS spectra were recorded on the representative polycrystalline and amorphous $Ir_{0.6}Co_{0.4}O_2$ samples. Fig. 5(a) shows the Co K-edge x-ray absorption near edge structure (XANES) spectra of both $Ir_{0.6}Co_{0.4}O_2$ samples compared to standard Y_2MnCoO_6 (Co^{2+}) and $LaCoO_3$ (Co^{3+}) references. As can be seen, the shape of the white line of the XANES
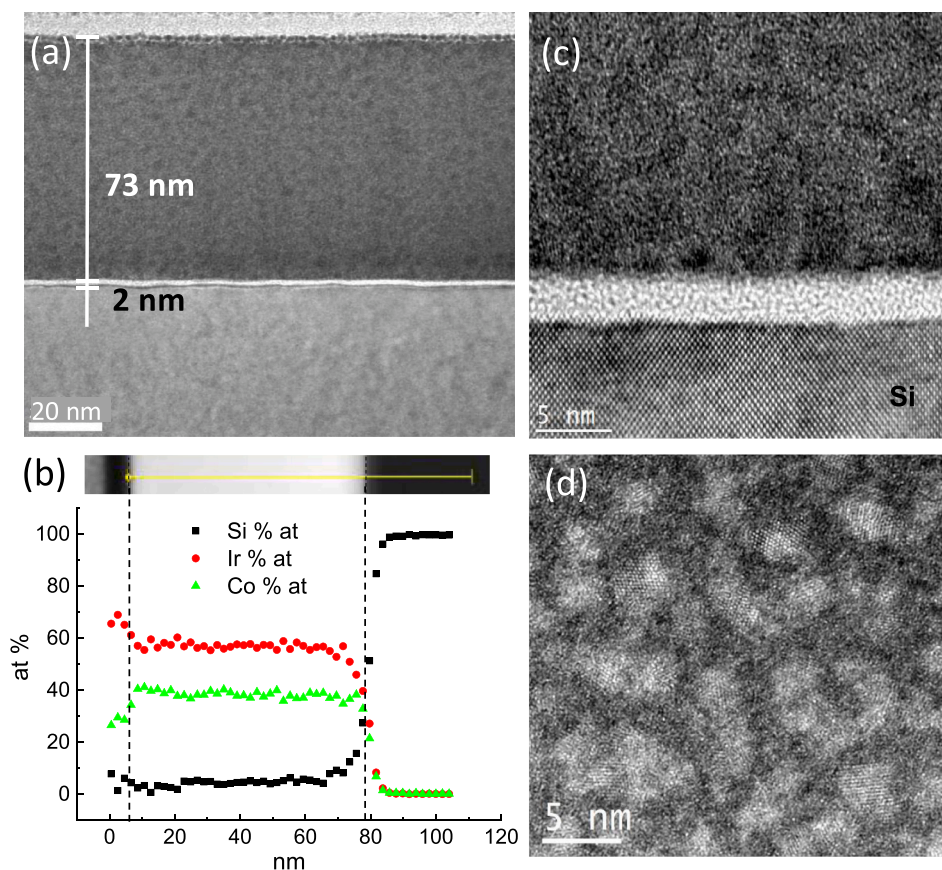
Fig. 2. (a) and (c) TEM/HRTEM images of cross-section corresponding to the as-grown 40 % Co-doped IrO2 film on silicon substrate. (b) EDS line-scan in situ STEM-HAADF quantifying the substitution of Ir by Co. (d) Image in HRSTEM-HAADF of a zoomed area of the annealed 40 % Co-doped IrO_2 film. The as-grown film is mainly amorphous while crystalline grains of ~ 4 nm size can be clearly discerned in the annealed one.

spectra corresponding to the Co-doped IrO_2 samples is wider than that of the Co^{3+} and Co^{2+} references. This is due to the differences in the crystal structure: even though in all the samples the Co ions are surrounded by oxygen octahedra, the different connections between octahedra (i.e. a combination of edge-sharing and corner-sharing for the rutile vs. only corner-sharing-octahedra in the case of the perovskite references) result in broader bandwidths and a more metallic character in the former. The random Ir/Co substitution further contributes to the broadening of the spectral features. This hinders a straightforward inference of the oxidation state based on the comparison of the edge positions. On the other hand, comparison of Fourier transforms (FT) of Co K-edge extended x-ray absorption fine structure (EXAFS) spectra in Fig. 5(b) clearly shows that the Co-O distance in the Co-doped IrO_2 samples matches that of $LaCoO_3$ reference whereas it is smaller than that of Y_2MnCoO_6. This points to a Co^{3+} oxidation state for the rutile films and rules out a substantial presence of Co^{2+} and/or Co^{4+} ions.

Comparing the XANES spectra recorded at the Ir $L_{2,3}$ edges (Fig. 6) on the polycrystalline $Ir_{0.6}Cr_{0.4}O_2$ and IrO_2 films a small shift of ~ 0.1 eV towards higher energy is observed in the doped film, indicating a reduction of the Ir-O distance for the Co-doped films relative to pure IrO2. This contraction is confirmed by the shift of the EXAFS features and the concomitant shift in the FT (see Fig. 6(b)). Interestingly, a clear increase of the integrated intensity is also observed at the white line of the Ir L2,3 edge XANES spectra. Such a distance reduction is expected to cause an increase of the hybridization with the oxygen orbitals that, in turn, results in a delocalization of the 5d states and a reduction in the integrated intensity of the white line in XANES. Therefore, the observed spectral modification indicates an increase in the number of holes in the Ir(5d) band as Co is introduced in the lattice, i.e. an increase in the oxidation state, in agreement with the results found at the Co K edge.

Given the 3+ oxidation state of cobalt ions a formal 5+ oxidation state would be expected for a 50 % substitution of Ir ions by Co. In the case of our $Ir_{0.6}Cr_{0.46}O_2$ samples a $4.7+$ oxidation state is inferred for Ir. A similar result is found for the amorphous samples (Fig. 6(c)).

The Ir (5d) ground-state expectation value of the angular part of the SOC, $\langle L \cdot S \rangle$, can be obtained by measuring the XAS branching ratio (BR $= IL_3/IL_2$, where $IL_{2;3}$ is the integrated white line intensity at a particular spin-orbit split edge) via BR $= (2 + \langle L \cdot S \rangle / n_h)/(1 - \langle L \cdot S \rangle / n_h)$, where n_h is the number of holes in the Ir(5d) band [35,35,36,36]. Assuming a formal 4.7 + oxidation state and, therefore, $n_h = 5.3$ the sum-rule analysis of the XAS spectra indicates a ~ 13 % increase of the $\langle L \cdot S \rangle$ for the $Ir_{0.6}Cr_{0.4}O_2$ samples (see Table 2).

To gain further information about the electronic occupancy of the Ir (5d) band and the origin of the increase observed in $\langle L \cdot S \rangle$ it is helpful to recall that: (i) the L_2 edge is exclusively sensitive to transitions involving $5d_{3/2}$ holes while the L_3 edge is sensitive to both $5d_{3/2}$ and $5d_{5/2}$ so that a higher BR indicates a higher $n_{h (5/2)}/n_{h (3/2)}$ ratio [37,38,37,38], (ii) in the limit of negligible spin-orbit coupling effects, the $J = 3/2$ and $J = 5/2$ multiplets will be degenerate yielding BR = 2; (iii) similarly, if the electronic bandwidth is large compared to the strength of the spin-orbit coupling, the overlap between the $J = 3/2$ and $J = 5/2$ multiplets can result in significantly reduced BR and $\langle L \cdot S \rangle$. As can be seen in Table 2, in the four films studied here, the BR departs from 2 indicating a non-negligible SOC and a primarily (but not purely) $5d_{5/2}$ rather than $5d_{3/2}$ character of the holes at the Ir(5d) band. Regarding the effect of doping, the increase of the integrated intensity at the L_2 observed in the Co-doped samples is found to cause a slight reduction of the BR. In other words, the Ir-Co hybridization broadens the electronic bandwidth and leads to a higher degree of $J = 3/2$ and $J = 5/2$ mixing in the 5d band (in the t_{2g} manifold). Despite of that, the increase in the number of
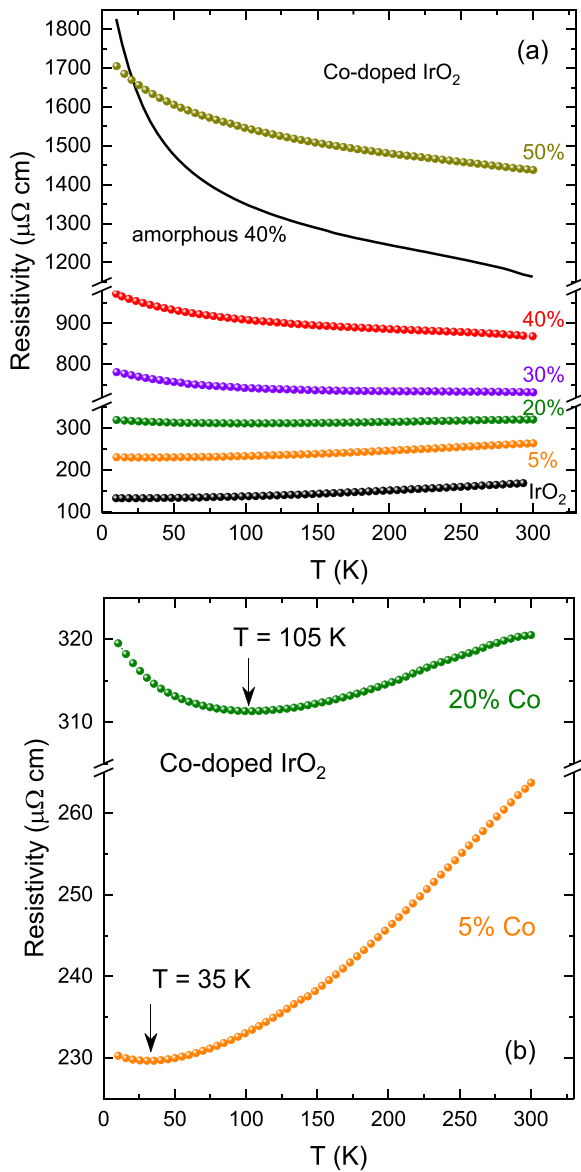
Fig. 3. (a) ρ(T) curves measured in the annealed $Ir_{1-x}Co_xO_2$ (0 < x < 60 range) and the amorphous $Ir_{0.6}Co_{0.4}O_2$ films, (b) zoomed image corresponding to the samples showing an upturn (marked with arrows).

unoccupied states overcomes this detrimental effect and results in an increase of the SOC ($\langle\mathbf{L}\cdot\mathbf{S}\rangle$).

It is instructive to note that this behavior is different to that found for Ir double perovskites [12,39] [12,39]. For those samples not only n_h but also the BR increases as we move from Ir^{4+} to Ir^{5+} (and the decreases again for Ir^{6+}). In the perovskites no change in the integrated intensity is observed at the L_2 edge but the spectral modification between Ir^{4+} and Ir^{5+} ions consists only on a shift towards higher energy, which indicates that the new unoccupied 5d state is purely $5d_{5/2}$. This difference is rooted in the different modification of the crystal structure: in the rutile structure substituting Ir by a smaller ion causes a contraction of the octahedra while in double perovskites there is mainly a tilting of the Ir-O-M angles that narrows the bandwidth. From this analysis the conditions that ideal dopant ions should fulfil in order to further optimize the performance of the IrO_2 as spin current detectors can be clearly inferred, namely, (i) 3 + or 2 + oxidation state to induce Ir^{5+} ions, (ii) larger size (but not too much) and (iii) a closed-shell configuration. From here, we propose Ga, In, Sc, Cu as good candidates.
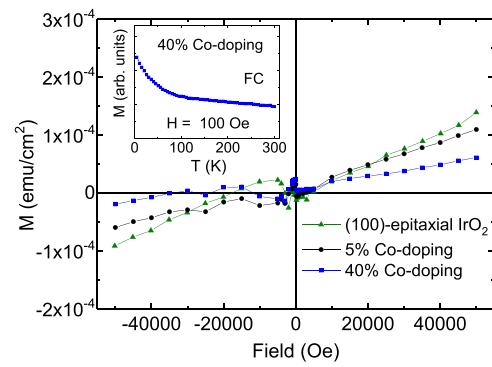

Fig. 4. M(H) curves recorded on two selected annealed $Ir_{1-x}Co_xO_2$ (x = 0.05, 0.4) samples at T = 5 K compared to that measured on a 100 nm-thick (100)-epitaxial IrO_2 thin film. Ideally, for a LS Co^{3+} (S=0) dopant, a magnetization proportional to the Ir content should be obtained. The observed deviation from this ideal behavior can be mainly associated to certain variability of the experimental conditions, such as a small signal/noise ratio and the dissimilar presence of silver paste used to glue the substrate during deposition. The inset shows the Field Cooled M(T) curve recorded on $Ir_{0.6}Cr_{0.4}O_2$ sample.

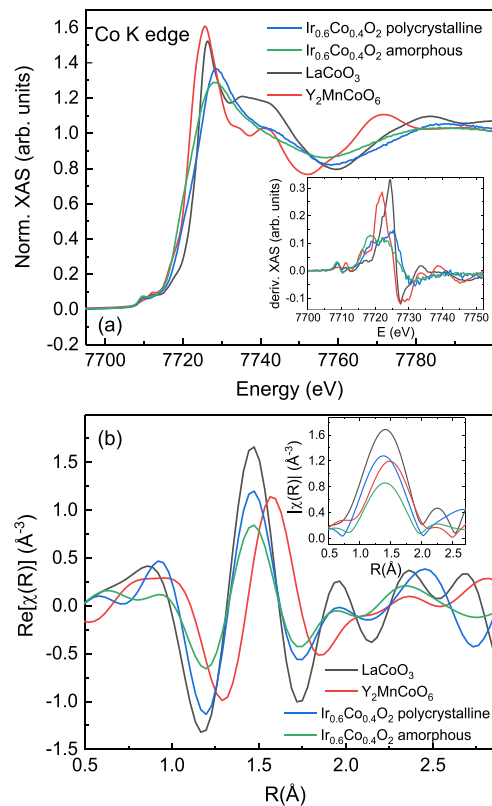**Fig. 5.** (a) Normalized Co K–edge XANES spectra recorded at RT on the polycrystalline and amorphous $Ir_{0.6}Cr_{0.4}O_2$, and references $LaCoO_3$ (Co^{3+}) and Y_2MnCoO_6 (Co^{2+}). The inset shows the first derivative XANES spectra (b) Real part of the FTs of the Co-K edge EXAFS signals (k-range from 3.0 to 8.0 Å−1; k^2-weighted; Hanning window, dk =0.5 Å^{-1}). In the inset, the modulus of the FTs is shown.

4. Conclusions

Polycrystalline $Ir_{1-x}Co_xO_2$ (0.05 $\leq$ x $\leq$ 0.6) thin films of ~70 nm have been successfully grown by reactive magnetron co–sputtering followed by an annealing treatment at 600 °C. The structural characterization shows that a rutile single phase is formed in all the samples, confirming that Ir and Co form a substitutional solid solution phase.
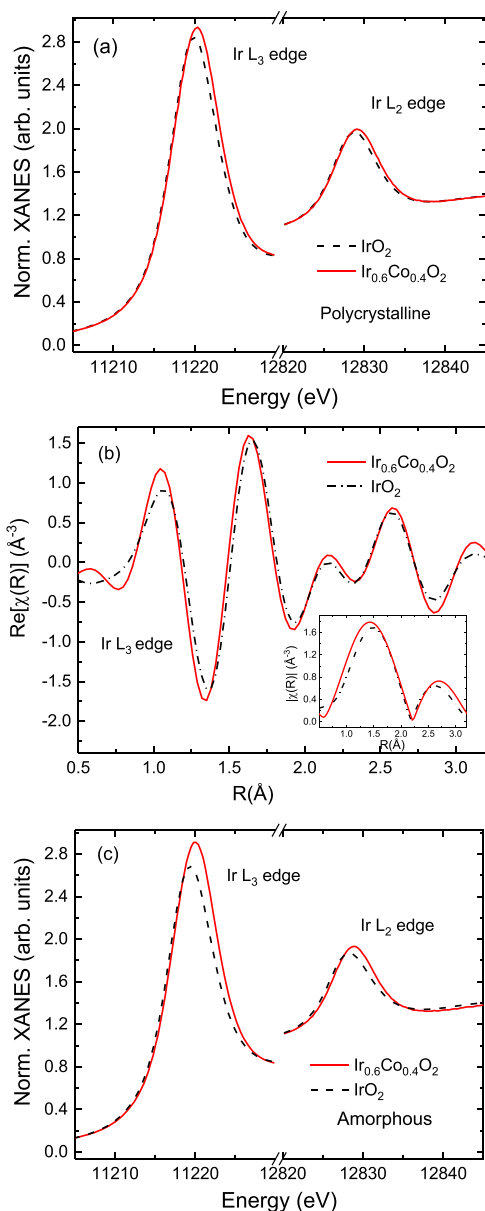
Fig. 6. (a) Normalized Ir $L_{2, 3}$–edges XANES spectra recorded at RT on the polycrystalline $Ir_{0.6}Cr_{0.46}O_2$ sample compared to that of pure IrO_2. (b) Corresponding FTs of the EXAFS signals (Real parts, k-range from 3.0 to 8.0 Å−1; k^2-weighted; Hanning window, dk =0.5 Å^{-1}). In the inset, the modulus of the FTs is shown. (c) Normalized Ir $L_{2, 3}$–edges XANES spectra recorded at RT on the amorphous $Ir_{0.6}Cr_{0.46}O_2$ sample compared to that of pure IrO_2.

Table 2

Summary of results obtained from XAS measurements: branching ratio and spin-orbit expectation value $\langle \mathbf{L \cdot S} \rangle$ in units of $\hbar^2$.

Sample	BR	$\langle \mathbf{L \cdot S} \rangle$
IrO_2 polycrystalline	3.88	1.93
IrO_2 amorphous	4.37	2.20
$Ir_{0.6}Cr_{0.4}O_2$ polycrystalline	3.85	2.18
$Ir_{0.6}Cr_{0.4}O_2$ amorphous	4.33	2.49

The electrical characterization of the $Ir_{1-x}Co_xO_2$ samples reveals an evolution from metallic to semiconductor–like response as Co content increases. The M(H) loops indicate a paramagnetic behavior, similar to that found in IrO_2, for all the $Ir_{1-x}Co_xO_2$ films. Neither ferromagnetism nor an enhanced paramagnetism is observed when Ir is partially substituted by Co.

The combined analysis of the XRD, ρ(T), M(H) and XAS data indicate that: (i) Co doping causes a lattice contraction, a reduction of the Ir-O bond distances and an increase of the Ir 5d bandwidth, (ii) the electronic configuration of Co ions is Co^{3+} $3d^6$ LS, so Co doping successfully induces an increase in the oxidation state of Ir (up to 5 + for 50 % doping), (iii) the increase in the oxidation state of Ir causes, in turn, an increase of the SOC, (iv) disorder is the main mechanism inducing the MIT in $Ir_{1-x}Co_xO_2$ samples.

Since the enhancement of the SOC is expected to lead to more efficient conversion of pure spin-currents on charge-currents, this work reveals the potential of $Ir_{1-x}Co_xO_2$ films to improve the performance of the IrO_2 as spin current detectors. The increase of the resistivity also contributes to this improvement. The study of this series also reveals that further optimization requires dopants that combine both a 3+ or 2+ oxidation state, so that a Ir^{5+} can be obtained, and a large ionic radius to reduce the bandwidth. Regarding the catalytic activity, the stabilization of IrO_2-like thin films containing both Ir^{5+} ions and large amount of leachable dopant provides a new playground for the optimization of the OER performance.

CRediT authorship contribution statement

M.A. Laguna–Marco: Conceptualization, Investigation, Supervision, Funding acquisition, Writing - original draft, Writing - review & editing. **J. Herrero-Albillos:** Investigation, Writing - review & editing. **M.H. Aguirre:** Investigation, Funding acquisition, Writing - review & editing. **M. Rueda-Jiménez:** Resources, Investigation, Visualization. **I. Mikulska:** Investigation, Writing - review & editing.

Declaration of Competing Interest

The authors declare that they have no known competing financial interests or personal relationships that could have appeared to influence the work reported in this paper.

Data Availability

Data will be made available on request.

Acknowledgments

References

[1] K. Fujiwara, Y. Fukuma, J. Matsuno, H. Idzuchi, Y. Niimi, Y. Otani, H. Takagi, Nat. Commun. 4 (2013) 2893.

[2] M. Morota, Y. Niimi, K. Ohnishi, D.H. Wei, T. Tanaka, H. Kontani, T. Kimura, Y. Otani, Phys. Rev. B 83 (2011), 174405.

[3] E. Arias-Egido, M.A. Laguna-Marco, C. Piquer, R. Boada, S. Díaz-Moreno, Adv. Funct. Mater. 29 (2019), 1806754.
[4] N. Che Ani, M.Z. Sahdan, N. Nayan, F. Adriyanto, K.M. Wibowo, Mater. Sci. Eng.: B 276 (2022), 115536.
[5] Vo. Van On, Chu Viet Ha, Dang Tuan Anh, J. Guerrero-Sanchez, D.M. Hoat, J. Phys.: Condens. Matter 34 (2022), 355301.
[6] N.A. Zarkevich, P. Singh, A.V. Smirnov, D.D. Johnson, Acta Mater. 225 (2022), 117477.
[7] H. Wan, X. Xiao, Y.S. Ang, Nanomaterials 12 (2022) 56.
[8] J.K. Harada, N. Charles, K.R. Poeppelmeier, J.M. Rondinelli, Adv. Mater. 31 (2019), 1805295.
[9] V.K. Dwivedi, S. Mukhopadhyay, J. Appl. Phys. 126 (2019), 165112.
[10] S. Mukherjee, D. Phuyal, C.U. Segre, S. Das, Olof Karis, T. Edvinsson, H. Rensmo, J. Phys. Chem. C 125 (2021) 14910.
[11] E. Arias-Egido, M.A. Laguna-Marco, C. Piquer, J. Chaboy, G. Fabbris, D. Haskel, Mater. Des. 196 (2020), 109083.
[12] M.A. Laguna-Marco, P. Kayser, J.A. Alonso, M.J. Martínez-Lope, M. van Veenendaal, Y. Choi, D. Haskel, Phys. Rev. B 91 (2015), 214433.
[13] J.M. Kahk, C.G. Poll, F.E. Oropeza, J.M. Ablett, D. Céolin, J.–P. Rueff, S. Agrestini, Y. Utsumi, K.D. Tsuei, Y.F. Liao, et al., Phys. Rev. Lett. 112 (2014), 117601.
[14] Y. Ping, G. Galli, W.A. Goddard, J. Phys. Chem. C 119 (21) (2015) 11570.
[15] W. Sun, Y. Song, X.Q. Gong, L.M. Cao, J. Yang, Chem. Sci. 6 (2015) 4993–4999.
[16] W.Q. Zaman, Z. Wang, W. Sun, Z. Zhou, M. Tariq, L. Cao, X.-Q. Gong, J. Yang, ACS Energy Lett. 2 (2017) 2786–2793.
[17] R.G. González-Huerta, G. Ramos-Sánchez, P.B. Balbuena, J. Power Sources 268 (2014) 69–76.
[18] H. Lee, J.Y. Kim, S.Y. Lee, J.A. Hong, N. Kim, J. Baik, Y.J. Hwang, Sci. Rep. 8 (2018) 16777.
[19] Y. Wang, S. Hou, R. Ma, J. Jiang, Z. Shi, C. Liu, J. Ge, W. Xing, ACS Sustain. Chem. Eng. 9 (2021) 10710–10716.
[20] Y. Wang, S. Hao, X. Liu, Q. Wang, Z. Su, L. Lei, X. Zhang, ACS Appl. Mater. Interfaces 12 (2020) 37006–37012.
[21] M. Elmaalouf, M. Odziomek, S. Duran, M. Gayrard, M. Bahri, C. Tard, A. Zitolo, B. Lassalle-Kaiser, J.Y. Piquemal, O. Ersen, C. Boissière, C. Sanchez, M. Giraud, M. Faustini, J. Peron, Nat. Commun. 12 (2021) 3935.
[22] D. González, M. Sodupe, L. Rodríguez-Santiago, X. Solans-Monfort, J. Catal. 412 (2022) 78–86.
[23] F. Scarpelli, N. Godbert, A. Crispini, I. Aiello, Inorganics 10 (2022) 115.
[24] H.N. Nong, T. Reier, H.S. Oh, M. Gliech, P. Paciok, T.H.T. Vu, D. Teschner, M. Heggen, V. Petkov, R. Schlögl, T. Jones, P. Strasser, Nat. Catal. 1 (2018) 841–851.
[25] G. Dennis, W. Helsby, D. Omar, I. Horswell, N. Tartoni, S. Hayama, I. Mikulska and S. Diaz-Moreno, AIP Conference Proceedings 2054, 2019, p. 060065.
[26] D. Von Dreifus, A.J.A. de Oliveira, A.V. do Rosario, E.C. Pereira, J. Supercond. Nov. Magn. 26 (2013) 2319–2321.
[27] H. Rollinson, J. Adetunji, Ionic Radii, in: W.M. White (Ed.), Encyclopedia of Geochemistry, Springer, Cham, 2018.
[28] J.H. Gruenewald, J. Nichols, J. Terzic, G. Cao, J.W. Brill, S.S.A. Seo, J. Mater. Res. 29 (2014) 2491–2496.
[29] G. Bergmann, Phys. Rep. 107 (1984) 1–58.
[30] H.Y. Qiao, H.M. Xiao, J.N. Meyer, C.M. Sun, A.A. Rouleau, D.B. Puretzky, I. N. Geohegan, M. Ivanov, W.J. Yoon, Weber, M.D. Biegalski, Mater. Chem. C1 (2013) 4628–4633.
[31] H. El Aakib, J.F. Pierson, M. Chaik, C. Samba Vall, H. Ait Dads, A. Narjis, A. Outzourhit, Vacuum 159 (2019) 346–352.
[32] Z.-X. Shen, J.W. Allen, P.A.P. Lindberg, D.S. Dessau, B.O. Wells, A. Borg, W. Ellis, J. S. Kang, S.-J. Oh, I. Lindau, W.E. Spicer, Phys. Rev. B 42 (1990) 1817.
[33] B. Fisher, D.S. Tannhauser, J. Chem. Phys. 44 (1966) 1663.
[34] S.M. Loya-Mancilla, P. Poddar, R. Das, H.E.E. Ponce, I.L. Templeton-Olivares, O. O. Solis-Canto, C.E. Ornelas-Gutierrez, F. Espinosa-Magaña, S.F. Olive-Méndez, Nanoscale Res. Lett. 9 (2014) 635.
[35] G. van der Laan, B.T. Thole, Phys. Rev. Lett. 60 (1988) 1977.
[36] M.A. Laguna-Marco, D. Haskel, N. Souza-Neto, J.C. Lang, V.V. Krishnamurthy, S. Chikara, G. Cao, M. van Veenendaal, Phys. Rev. Lett. 105 (2010), 216407.
[37] B. Qi, I. Perez, P.H. Ansari, F. Lu, M. Croft, Phys. Rev. B 36 (R) (1987) 2972–2975.
[38] J.P. Clancy, N. Chen, C.Y. Kim, W.F. Chen, K.W. Plumb, B.C. Jeon, T.W. Noh, Y.- J. Kim, Phys. Rev. B 86 (2012), 195131.
[39] M.A. Laguna-Marco, E. Arias-Egido, C. Piquer, V. Cuartero, L. Hernández-López, P. Kayser, J.A. Alonso, J.A.T. Barker, G. Fabbris, C.A. Escanhoela Jr., et al., Phys. Rev. B 101 (2020), 014449.